Journal of Advanced Marine Engineering and Technology, Vol. 49, No. 3, pp. 168~178, 2025
J. Advanced Marine Engineering and Technology (JAMET)
https://doi.org/10.5916/jamet.2025.49.3.168

ISSN 2234-7925 (Print)
ISSN 2765-4796 (Online)
Original Paper

Effects of circular cylinder rotating ratios on wake vortex suppression using OpenFOAM

Hongwu Zhao[1] · Jun Ho Jeon[2] · Dong In Yu[3] · Yeon Won Lee[†]

(Received June 4, 2025 ; Revised June 17, 2025 ; Accepted June 23, 2025)

Abstract: Columnar structures are widely used in wind, offshore and marine engineering. These structures are often subjected to vortex-induced vibrations (VIV), which can lead to fatigue damage in severe cases. In this study, the open-source software Open-Source Field Operation and Manipulation (OpenFOAM) is used to simulate fluid flow around a rotating circular cylinder and examined the effects of different rotation ratios on the wake of the cylinder. The objective of this study is to explore the possibility of suppressing vortex-induced vibrations by controlling the swirling flow around the cylinder. Our large-eddy simulation (LES) results show that the streamwise turbulent flow exhibits non-linear changes as the cylinder's rotation ratio increases. The vortex structure weakens and becomes less coherent as the cylinder's rotating speed increases, and the influence of spanwise vortices diminishes. Furthermore, as the rotating ratio(α) increases, the lift coefficient shows an overall rising trend, whereas the drag coefficient initially decreases and then gradually increases. The Strouhal number decreases and eventually reaches zero, indicating that vortex shedding is effectively suppressed. In summary, generating a swirling flow around the cylinder by rotation can effectively suppress the formation and periodic shedding of vortices from the cylinder.

Keywords: Vortex-induced vibration (VIV), Rotating cylinder, Large-eddy simulation (LES), Wake flow, Flow control, Computational fluid dynamics (CFD)

Nomenclature

U	Velocity	CW	WALE model constant coefficient
$U\infty$	Far field velocity	Ck	WALE model constant coefficient
P	Pressure	Cc	WALE model constant coefficient
ρ	Density	Re	Reynolds number
$\hat{U}$	Filtered velocity	D	Cylinder diameter
$\bar{p}$	Filtered pressure	Δz	Spanwise length
t	Time	νt	Sub-grid viscosity
ν	Kinematic viscosity	Nr	Nodes number in radial direction
τij	Sub-grid scale stress tensor	$N\theta$	Nodes number in tangential direction
Sij	Traceless symmetric part of square of the velocity gradient tensor	Cd	Average value of drag coefficient
		St	Strouhal Number
$\tilde{\eta}ij$	Traceless antisymmetric part of square of the velocity gradient tensor	Cl	Average value of lift Coefficient
		α	Rotating ratio
Δ	The characteristic size of mesh	$t*$	Dimensionless time
$\hat{O}P$	The specific operation in WALE model	ω	Rotating speed

† Corresponding Author (ORCID: https://orcid.org/0000-0002-3749-8119): Professor, School of Mechanical Engineering, Pukyong National University, 45, Yongso-ro, Nam-gu, Busan, Korea, E-mail: ywlee@pknu.ac.kr, Tel: 051-629-6162

1 Assistant Professor, Zhejiang University of Water Resources and Electric Power, E-mail: angellice@163.com

2 Researcher, School of Mechanical Engineering, Pukyong National University, E-mail: skya333@naver.com.

3 Associate Professor, School of Mechanical Engineering, Pukyong National University, E-mail: diyu@pknu.ac.kr.

Fx	The total force per unit length in the positive direction of X axis
Fy	The total force per unit length in the positive direction of Y axis
ϵ	Characteristics area
fs	Dimensionless vortex shedding frequency

1. Introduction

Leonardo da Vinci was among the first to observe turbulent flow patterns in water as early as the Renaissance period **[1]**. Later, Osborne Reynolds demonstrated through experiments that the onset of turbulence is governed by a certain dimensionless parameter now known as the Reynolds number **[2]**. Von Kármán's studies of flow around a cylinder led to the conceptualization of the Kármán vortex street, which has since become a foundational phenomenon in fluid mechanics. Flow around circular cylinders has been the subject of extensive research for decades **[3]**. Zdravkovich identified various parameters that affect the flow characteristics, including the aspect ratio, surface roughness, diameter variation, blockage effects, wall proximity, boundary layer manipulation, yaw angle of the cylinder, and interference effects in multi-cylinder arrangements **[4]**. Early studies often focused on specific Reynolds numbers or geometric influences. For instance, Lienhard's experiments in 1966 explored how cylinder shape affects the wake **[5]**, while Norberg in 1994 examined the effect of aspect ratio at Re = 3900 **[6]**. Other studies analyzed the turbulent wake in greater detail using techniques such as direct numerical simulation (DNS) and particle image velocimetry (PIV). For example, Kravchenko and Moin [7] employed DNS, whereas PIV data by Lourenco and Shih, as reported in [7], were used to study vortex dynamics in the wake.

With advancements in computational fluid dynamics (CFD), a range of simulation techniques—from steady-state Reynolds-averaged Navier–Stokes (RANS) to transient LES and DNS—have been used to investigate flow past cylinders. Benim *et al.* **[8]** evaluated different turbulence models and confirmed that LES results agreed well with experimental data. LES-based investigations by Lysenko *et al.* **[9]** (using the dynamic Smagorinsky model) and Zhang *et al.* **[10]** (using the basic Smagorinsky model), as well as DNS work by Dong and Karniadakis **[11]**, have further enriched the database of flow characteristics for a stationary cylinder.

In contrast, studies on rotating cylinders have predominantly focused on either low Reynolds numbers (e.g., Re ≈ 200) or very high Reynolds numbers (e.g., on the order of 10^5). For instance, Seyed-Aghazadeh and Modarres-Sadeghi **[12]** conducted low-Re experiments; Mittal and Kumar **[13]**, as well as Thakur *et al.* **[14]**,

performed simulations under similar low-Re conditions. At the high Reynolds number range, Chen and Rheem **[15]** investigated rotating-cylinder flow at near-critical Reynolds numbers (~10^5).

Although Re = 3900 has become a canonical benchmark for stationary cylinder studies, rotating cylinders at this subcritical Reynolds number have received limited attention.

Furthermore, most of the existing studies at moderate Reynolds numbers have concentrated on overall force coefficients, while comparatively fewer works have addressed the wake dynamics—such as the evolution of Strouhal number, suppression of vortex-induced vibration, or three-dimensional vortex structures induced by rotation. Therefore, in this study, we numerically investigate the flow around a rotating circular cylinder at Re = 3900 using LES.

Vortex-induced vibration (VIV) is the oscillatory motion of bluff bodies, such as cylinders, caused by alternating lift forces from periodic vortex shedding. If uncontrolled, it can lead to structural fatigue. The Magnus effect refers to lift generated on a rotating body due to asymmetric pressure distribution. Cylinder rotation can alter wake structures and potentially suppress VIV.

Based on these principles, we investigate the development of wake turbulence, the evolution of three-dimensional vortex structures, the behavior of lift and drag coefficients, and the variation of the Strouhal number as functions of the rotation ratio.

This work aims to demonstrate the effectiveness of cylinder rotation as a control strategy for suppressing VIV in the Magnus type wind turbine.

2. Numerical Analysis

OpenFOAM **[21]**, an open-source CFD toolbox, employs the finite volume method to solve the governing equations. The computational domain is discretized into control volumes, and surface integrals are converted into volume integrals using the Gauss divergence theorem. Time integration is performed with a second-order implicit Crank–Nicolson scheme, and pressure–velocity coupling is handled via the PISO algorithm. In this study, the velocity field is solved using a preconditioned bi-conjugate gradient (PBiCG) solver with a residual tolerance of 1×10^–6, and the pressure field is solved using a geometric agglomerated algebraic multigrid (GAMG) solver, also with a residual tolerance of 1×10^{-6}.

Validation results for a stationary cylinder at Re = 3900 are presented separately in Section 2.3 to confirm the accuracy of the Wall-Adapting Local Eddy-viscosity (WALE) LES model. Simulations are then extended to rotating cylinder cases. The flow structures, vortex dynamics, and force coefficients are analyzed based on the computed results.

2.1 Governing Equations and Turbulence Models

For an incompressible, Newtonian fluid flow, the governing continuity and momentum equations are:

$$\nabla \cdot U = 0 \tag{1}$$

$$\frac{\partial U}{\partial t} + \nabla \cdot (U\boldsymbol{U}) = -\frac{\nabla P}{\rho} + \nabla \cdot (\nu \nabla U) \tag{2}$$

where U is the velocity vector, P is the pressure, ρ is the fluid density, and ν is the kinematic viscosity.

In 1963, Smagorinsky introduced the concept of Large Eddy Simulation (LES) **[16]**. Unlike Reynolds-Averaged Navier-Stokes (RANS) that model all turbulent scales, LES resolves large-scale turbulence explicitly while modeling only the smaller, subgrid-scale (SGS) motions. Several SGS models exist, including the standard Smagorinsky model, the dynamic Smagorinsky model, and the WALE model. The filtered form of the Navier–Stokes equations for LES is:

$$\nabla \cdot \tilde{u} = 0 \tag{3}$$

$$\frac{\partial \bar{u}}{\partial t} + \nabla \cdot (\bar{u}\bar{u}) = -\nabla \bar{P} + \nabla \cdot (\nu \nabla \bar{u}) - \nabla \cdot \tau, \tag{4}$$

where $\bar{u}$ and $\bar{P}$ are the filtered velocity and pressure, respectively, and $\tau_{ij} = \overline{u_i u_j} - \bar{u}_i \bar{u}_j$ is the subgrid-scale stress tensor.

The WALE model **[17]** is an algebraic (zero-equation) eddy-viscosity model. It accounts for both strain and rotation rates of the filtered velocity field, ensuring that the eddy viscosity vanishes near walls. This enhances prediction accuracy in transitional and near-wall regions **[18][19]**. The WALE model computes the eddy viscosity ν_t as:

$$\nu_t = \left(C_w \Delta\right)^2 \frac{\left(S_{ij}^d S_{ij}^d\right)^{3/2}}{\left[\left(S_{ij}S_{ij}\right)^{5/2} + \left(S_{ij}^d S_{ij}^d\right)^{5/2}\right]} \tag{5}$$

With:

$$S_{ij}^d = \overline{S_{ij}}\,\overline{S_{jk}} + \overline{\Omega}_{ij}\,\overline{\Omega}_{ij} - \frac{1}{3}\delta_{ij}\left[\overline{S_{mn}}\,\overline{S_{mn}} - \overline{\Omega}_{mn}\,\overline{\Omega}_{mn}\right] \tag{6}$$

Here, $\overline{S}_{ij}$ denotes the filtered strain rate tensor, $\overline{\Omega}_{ij}$ is the filtered rotation rate tensor, and δ_{ij} is the Kronecker delta. All quantities are computed from the filtered velocity field, consistent with LES methodology. The implementation is available in OpenFOAM **[21]**.

2.2 Computational Setup and Boundary Conditions

This study used a structured O-grid mesh to generate the computational domain and cylinder geometry, as shown in **Figure 1**. The circular cylinder is located at the center of the domain. **Figure 1** provides an overview of the computational domain and mesh structure used in the simulations. Following prior studies **[7][9][20]**, the spanwise domain length (along the cylinder axis) is set to πD, which is adequate for capturing the dominant wake structures at Re = 3900. (For more complex flows, such as those involving yawed cylinders **[22]**, longer domains may be needed.)

The freestream velocity is set to Re = 3900 based on the cylinder diameter D and the kinematic viscosity of the fluid. At the outlet, a zero-gradient condition is applied for velocity, and pressure is fixed to zero (gauge). The cylinder surface uses a no-slip wall condition. For rotating cases, a constant angular velocity ω is applied about the cylinder axis (z-axis), with clockwise rotation when viewed from above. The rotation ratio is defined as:

$$\alpha = \frac{\omega R}{U_\infty} \tag{7}$$

where ω is the angular rotation speed of the cylinder, R is the cylinder radius (D/2), and U_∞ is the free-stream velocity. Simulations are conducted for various α.

No wall functions are used; the near-wall flow is fully resolved down to the viscous sublayer. Symmetry boundary conditions are applied at the spanwise domain boundaries implying symmetry in the z-direction.

The simulation for the stationary case ($\alpha = 0$) is run first until a statistical steady state is achieved. The resulting flow field is used as the initial condition for all $\alpha > 0$ cases. Cylinder rotation ($\alpha > 0$) begins after 500 s of simulated time under stationary ($\alpha = 0$) conditions, ensuring the flow is fully developed before rotation. The non-dimensional time t^* is defined as:

$$t^* = \frac{U(t-500)}{D} \tag{8}$$

so that $t^* = 0$ corresponds to the start of rotation. The time step is chosen to maintain the Courant number below 1.

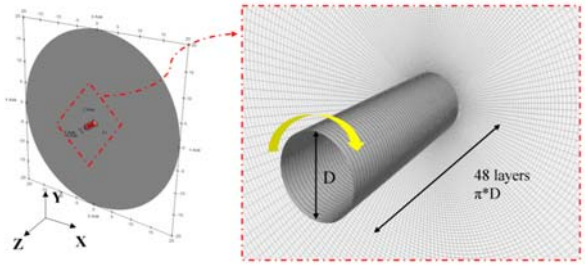

Figure 1: A complete sketch of computational domain and mesh

Table 1: Boundary Conditions

Position	Type	Condition
Inlet	Velocity	Fixed with turbulence intensity
Outlet	Pressure	Fixed
	Velocity	Zero gradient
Cylinder surface	Wall	No-slip
Spanwise boundaries	Symmetry plane	Symmetry

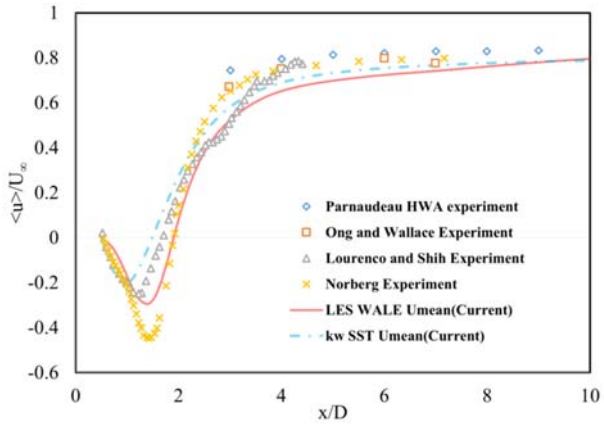

Figure 2: Streamwise Velocity on the center line in the wake of cylinder

Throughout the simulations, drag and lift coefficients (C_D and C_L) are recorded. The Strouhal number (St) is determined via Fast Fourier Transform (FFT) of the lift coefficient signal. The

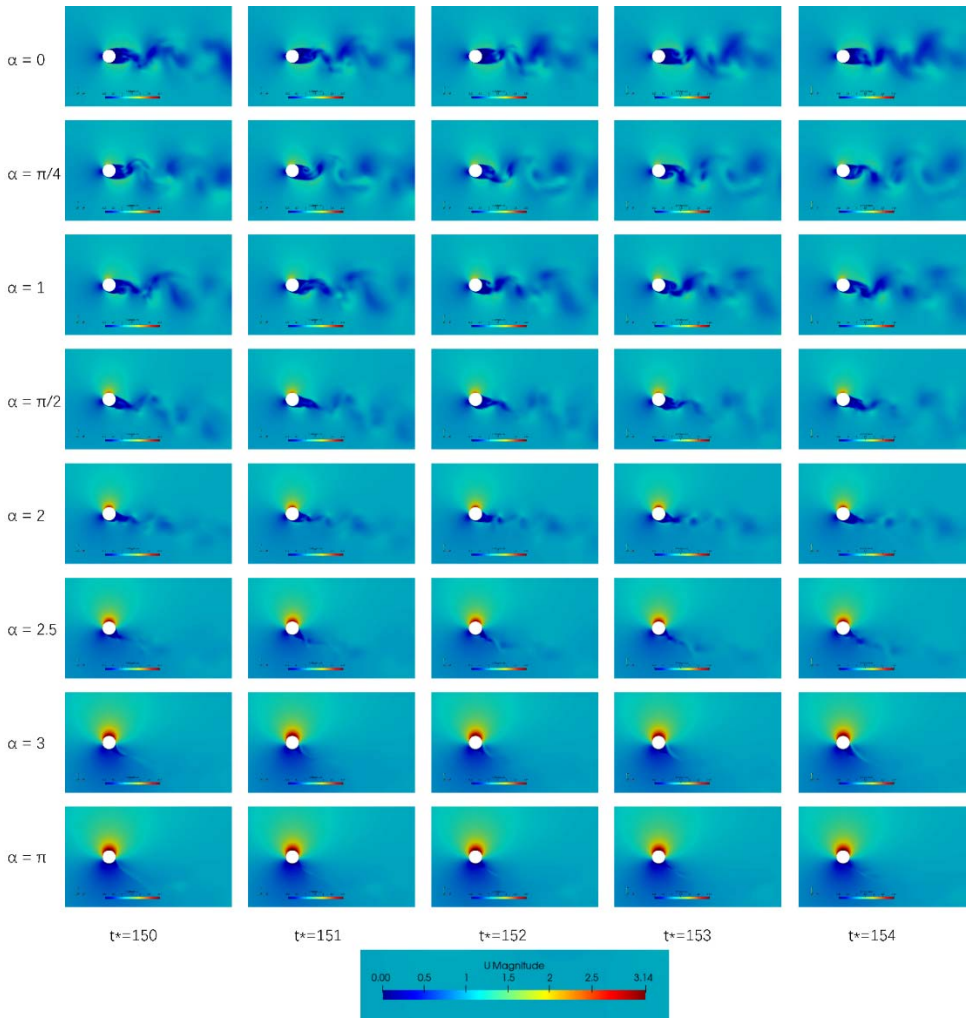

Figure 3: Snapshots of instantaneous streamwise velocity (α = 0 ~ π)

following definitions are used for computing these quantities:

$$C_D = \frac{F_x}{(0.5\rho U^2 A)} \quad (9)$$

$$C_L = \frac{F_y}{(0.5\rho U^2 A)} \quad (10)$$

$$St = f_s D/U \quad (11)$$

where F_x and F_y are the total drag and lift forces per unit length (acting in the positive X and Y directions, respectively), A is the characteristic area (projected frontal area of the cylinder, equal to D×1 for a unit span), and f_s is the vortex shedding frequency. **Table 1** below summarizes the boundary conditions applied in the simulation.

2.3 Validation and Verification

To evaluate the accuracy of the numerical approach, the simulation results for a stationary cylinder at Re = 3900 were compared with well-known experimental and numerical data from the literature. **Figure 2** shows the streamwise velocity along the wake centerline, demonstrating good agreement with the experimental measurements. Additionally, **Figure 3** illustrates a sequence of instantaneous streamwise velocity contours over one vortex shedding cycle for the stationary cylinder, further verifying the model's ability to capture periodic shedding phenomena. **Table 2** presents the mesh independence test results and a turbulence model comparison. The first part of the table shows time-averaged force coefficients and Strouhal number for three mesh resolutions using the LES WALE model. The Strouhal number (St) difference between the medium and fine grids is only 0.46%, indicating excellent agreement. Therefore, the medium mesh (2.3 million cells) is selected for subsequent simulations to balance accuracy and computational cost. The second part compares results using different SGS turbulence models (all at the medium mesh resolution). The differences among the models were within 3%, and the WALE model was employed in the present simulations.

Collectively, these validation and verification results demonstrate that the numerical approach (using the medium mesh and the WALE LES model) captures the main wake dynamics and vortex shedding behavior at Re = 3900 with sufficient accuracy. Some small-scale turbulence under strong rotation, however, may remain under-resolved and could be explored in future studies using finer grids.

3. Results and Discussion

Table 3 summarizes the time-averaged drag and lift coefficients, as well as the Strouhal number, for various rotation ratios α. These values are obtained from the long-time statistics of the flow after reaching quasi-steady state at each rotation rate:

As shown in **Table 3**, increasing the rotation ratio α leads to significant changes in the aerodynamic coefficients and the Strouhal number. The drag coefficient C_D decreases steadily with α up to around α = 2.5, reaching a minimum value of about 0.28 (a reduction of roughly 70% from α = 0). Beyond α ≈ 2.5, C_D shows a slight increase **[23]**. In contrast, the lift coefficient C_L increases monotonically with α due to the Magnus effect, attaining large positive values (e.g., C_L ≈ 10.62 at α = π). Meanwhile, the Strouhal number St, which characterizes the vortex shedding frequency, declines with increasing α and effectively approaches zero at high rotation rates (St is essentially 0 by α = 2.5 and above). These quantitative trends suggest that cylinder rotation strongly alters the wake flow dynamics, as discussed in detail below.

For a stationary cylinder (α = 0), the near wake is characterized by an alternating vortex shedding pattern, forming the classical von Kármán vortex street downstream. As α increases from 0, the wake flow becomes increasingly affected by the imposed swirl.

Table 2: Mesh independence Test and Turbulence Model Comparison

Grid Level	Cell No.	Turbulence Model	C_D (avg)	C_L (avg)	St
Coarse	1.2M	WALE	1.02	0.63	0.213
Medium	2.3M	WALE	0.997	0.6	0.216
Fine	4.6 M	WALE	0.994	0.59	0.217

Grid Level	Cell Count	Turbulence Model	C_D (avg)	C_L (avg)	St
Medium	2.3M	WALE	0.997	0.6	0.216
Medium	2.3M	Smagorinsky	1.05	0.71	0.222
Medium	2.3M	Dynamic Smagorinsky	1.01	0.66	0.218

Table 3: Time-averaged drag/lift coefficients and Strouhal number for various

Rotation Ratio (α)	Mean C_D	Mean C_L	Strouhal Number
0	0.99	0	2.19
Pi/4	0.91	1.13	0.24
1	0.78	1.53	0.29
Pi/2	0.44	3.1	0.19
2	0.33	4.78	0.19
2.5	0.28	7.21	0.098
3	0.37	9.85	-
pi	0.42	10.62	-

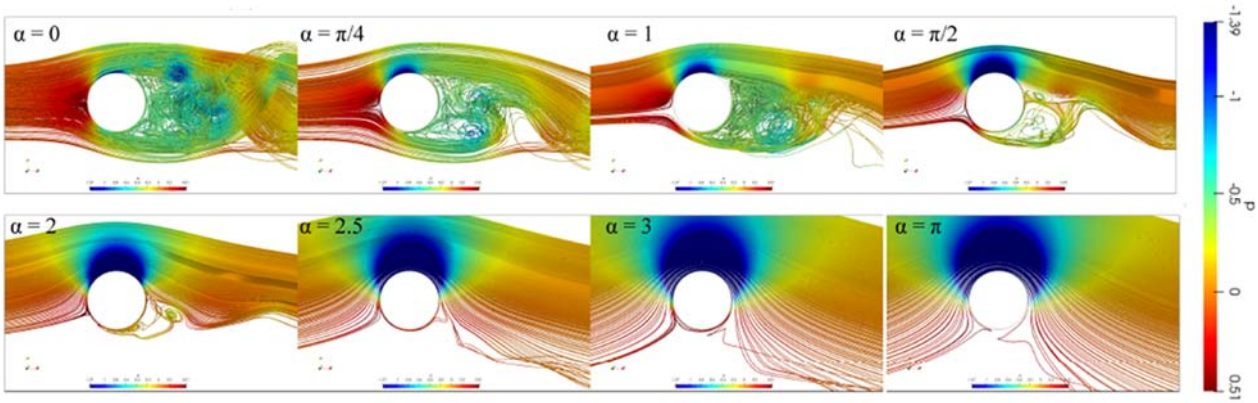

Figure 4: Flow field visualizations at various rotation ratios instantaneous streamlines overlaid with pressure contours

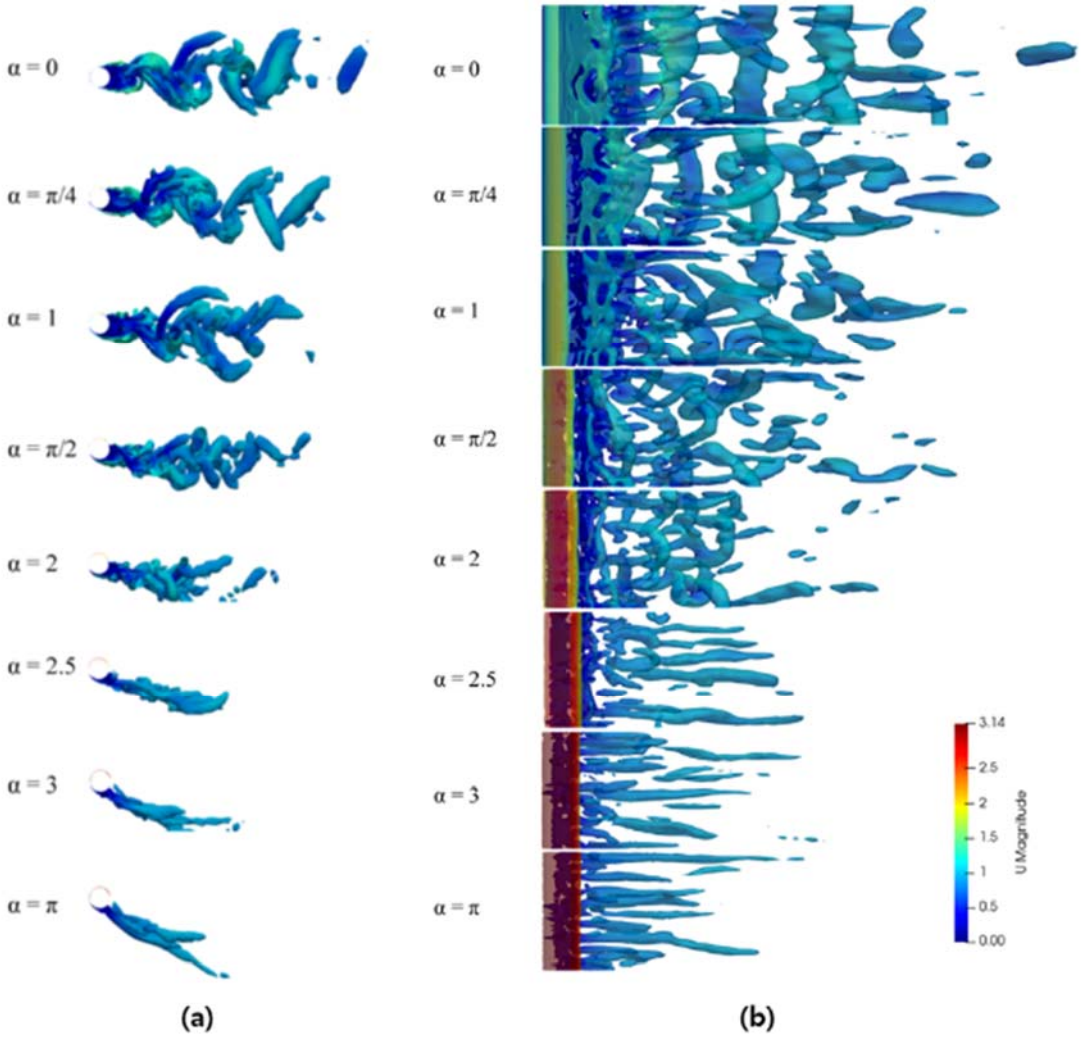

Figure 5: Iso-surfaces of Q-criterion (Q = 0.1) colored by velocity, for varying α values
(a) Side view in X–Y plane, (b) Top view in X–Z plane.3.1 Visualization of wake flow structure

Figure 4 shows instantaneous pressure contours and streamlines for various rotation ratios. At α = 0, periodic vortex shedding occurs about the centerline.

At a moderate rotation (e.g., α = 1), the wake becomes asymmetric: the shear layer on one side (depending on rotation direction) is energized by the moving surface, while the opposite-side shear layer

is weakened. This results in a biased wake with uneven vortex strengths. Visualizations illustrate that as the rotation ratio α increases, the periodic vortex pattern gradually disappears. At higher rotation ratios, the wake flow structure is dramatically altered. **Figure 5** presents the vortex cores visualized using the Q-criterion (an iso surface of the second invariant of the velocity gradient, Q = 0.1 is shown) for rotation ratios ranging from 0 up to α = π (approximately 3.14). In the stationary case (α = 0), we observe a street of staggered vortex tubes shedding periodically behind the cylinder. As α increases to π/4, 1, and π/2, the shed vortices diminish in strength and coherence. By α = 2.0, the vortices in the wake have lost much of their organized structure and appear more diffuse and elongated in the streamwise direction (indicating reduced three-dimensionality in the vortex loops). At α = 2.5 and above, the wake no longer shows a clear periodic vortex street; instead, the flow appears increasingly steady and no distinct vortex shedding is observed.

As α increases, the strength and coherence of the shedding vortices (blue and red vortex tubes) diminish. By α ≈ 2.5, the organized vortex street has effectively vanished, indicating a suppression of periodic vortex shedding. Overall, the wake flow visualization confirms that cylinder rotation progressively disrupts the formation of the Kármán vortex street. At sufficiently high rotation ratios, the wake becomes largely steady with attached or only slowly drifting vortical structures, instead of shedding vortices.

The suppression of periodic shedding can be further understood by examining the instantaneous and mean vortex structures in the wake. For rotating cases, the strong flow energy introduced by the moving surface create a stabilizing effect on the near-wake shear layers. In addition, the rotation produces a spanwise component of vorticity that interacts with the streamwise vortices, promoting earlier breakdown of coherent vortex loops. At α = 0, the wake vortices roll up alternately from each side of the cylinder and keep coherent structure over several diameters downstream. With small rotation (α = π/4 or 1), the vortices shed from the advancing side (the side moving with the flow) become stronger and those from the retreating side are weaker, yielding an asymmetrical vortex street. As α increases further, the weaker vortices are increasingly unable to form, while the stronger side vortices are convected away and dissipated faster due to enhanced small-scale mixing. By α ≈ 2.0, the classical vortex street pattern has nearly disappeared; the wake is dominated by a broad region of recirculating flow with only remnants of vortical structures. The effective wake length (the distance downstream where

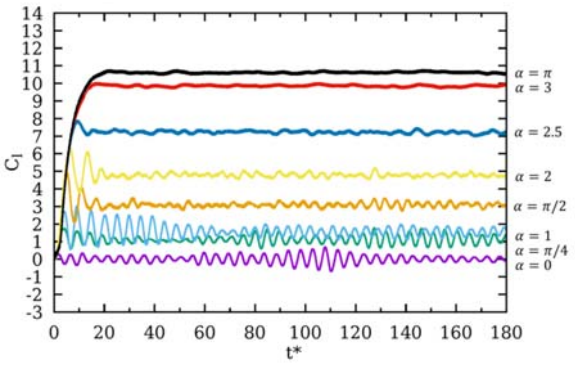

Figure 6: Time history of lift coefficient (C_l) for various α

significant vortices exist) shortens with increasing α, and the lateral spread of the wake increases (more diffusion), indicating that the organized energy of the vortex street is being converted into smaller-scale turbulence. In summary, as the rotation ratio increases, the wake vortex structure demonstrates a clear fading trend in coherence and strength. Beyond a threshold rotation rate (around α = 2.5 in our study), the flow does not shed regular vortices at all (contrast to the vigorous vortex street observed at α = 0.)

3.2 Analysis of Vortex Shedding

A time-domain analysis of the aerodynamic force coefficients provides further insight into how rotation influences unsteady loading on the cylinder. As shown in **Figure 6**, in the stationary case (α = 0), the lift coefficient C_L(t) exhibits a pronounced periodic oscillation around zero. As α increases, these oscillations are reduced. At α = 0, C_L oscillates sinusoidally due to alternating vortex shedding. By α = π/2, the amplitude of C_L oscillations are significantly lower. When α reaches 2.5, the lift oscillation is almost entirely gone – $C_L$becomes nearly a steady positive value

Figure 7 presents the frequency spectra (via FFT) of the lift coefficient signals for various rotation ratios. In the stationary case, a strong spectral peak is observed corresponding to the Strouhal frequency (St ≈ 0.21). As α increases, this peak's magnitude decreases and its frequency shifts slightly lower. By α = 2.5, the dominant peak in the spectrum has virtually vanished, indicating the absence of a periodic shedding frequency. The FFT analysis confirms that the vortex shedding frequency (and thus St) decreases with increasing rotation ratio and is effectively zero (no distinct shedding) for sufficiently high α. These observations are quantitatively consistent with the values given in **Table 3**.

Figures 8 and **9** plot the mean drag coefficient, mean lift coefficient, and Strouhal number, respectively, as functions of α. The mean drag coefficient (C_D) decreases steadily with α, reaching a

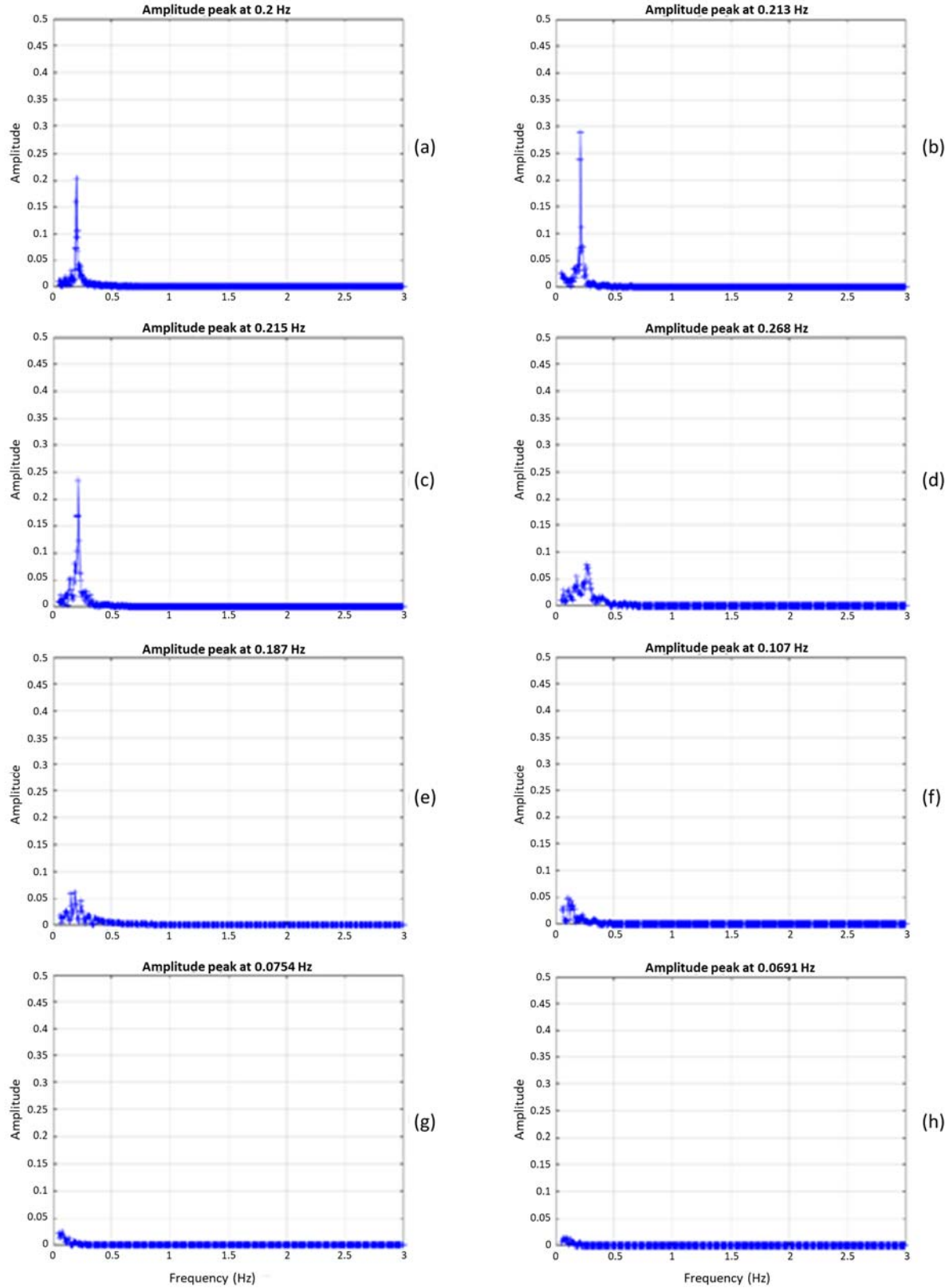

Figure 7: FFT analysis of lift coefficient (C_l) for various α

(a) $\alpha = 0$, (b) $\alpha = \pi/4$, (c) $\alpha = 1$, (d) $\alpha = \pi/2$, (e) $\alpha = 2$, (f) $\alpha = 2.5$, (g) $\alpha = 3$, (h) $\alpha = \pi$

minimum at α ≈ 2.5, followed by a slight increase at α = 3. In contrast, the mean lift coefficient (C_L) increases monotonically with α due to the Magnus effect (since the cylinder's rotation creates a lift force). The Strouhal number decreases sharply and then

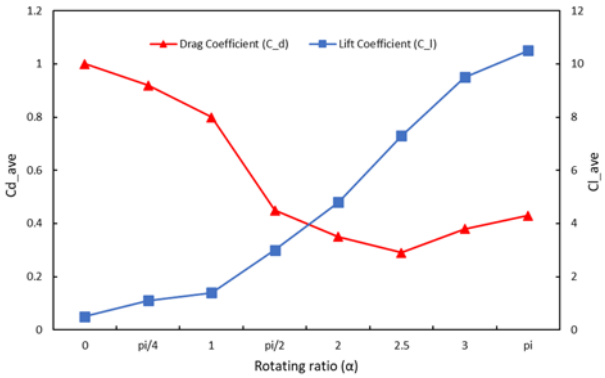

Figure 8: Time-averaged drag and lift coefficients as functions of rotating ratio α

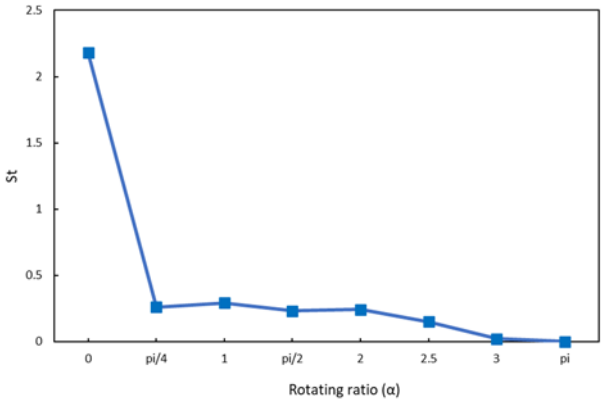

Figure 9: Variation of Strouhal number with rotating ratio α

gradually declines toward zero as α increases, confirming the suppression of periodic vortex shedding at high rotation rates. In summary, the time-averaged and fluctuating lift force coefficient data show that cylinder rotation can dramatically reduce unsteady aerodynamic forces. By $\alpha \approx 2.5$, the oscillatory lift force associated with VIV are almost completely eliminated.

These results show that rotating a cylinder at a sufficiently high ratio suppresses unsteady VIV by effectively disrupting the vortex shedding mechanism.

4. Conclusion

This study investigated the effects of cylinder rotation on wake flow characteristics and VIV through large-eddy simulations (LES) at a Reynolds number of 3900. The rotating circular cylinder was examined over a range of rotation ratios to analyze changes in wake flow structure, vortex shedding dynamics, and aerodynamic forces.

The results demonstrated that increasing the rotation ratio significantly altered the wake flow dynamics. At low rotation ratios (near $\alpha = 0.5–1.0$), the fluid flow exhibited periodic vortex shedding characteristic of a von Kármán vortex street, but with some asymmetry.-As the rotation increased, the wake flow became increasingly asymmetric and disorganized, with a reduction in vortex strength and spanwise coherence.

For rotation ratios of approximately 2.0–2.5 and above, periodic vortex shedding was almost completely suppressed.

Quantitative analysis revealed that the Strouhal number (vortex shedding frequency) decreases sharply and then decreases monotonically with increasing rotation ratio, effectively approaching zero at high rotation rates. The mean drag coefficient was reduced about 70% at $\alpha = 2.5$ compared to the non-rotating case, before rising slightly at the highest rotation ($\alpha = 3.0$). Meanwhile, the mean lift coefficient increased significantly due to the Magnus effect, reaching several times the non-rotating value at the highest rotation rate.

In summary, cylinder rotation was shown to be an effective method for suppressing vortex-induced vibrations by weakening and eventually eliminating periodic vortex shedding. By generating a sustained swirling flow around the cylinder, rotation disrupts the formation of coherent vortices in the wake. These findings provide a foundation for further exploration of flow control strategies in Magnus type wind applications, where mitigating VIV is crucial for structural longevity and safety. To support this goal, future work will include FSI-based high-fidelity analysis and power requirement estimation.

Acknowledgement

This paper is a revised version of a paper entitled “A numerical study on the suppression of vortex shedding around a cylindrical structure using active and passive control approaches” presented at ICTAM2024, August 25-30, 2024, Daegu, Korea. And this work was supported by a Research Grant of Pukyong National University (2023).

Author Contributions

Conceptualization, H. Zhao and Y. W. Lee; Methodology, H. Zhao and J. H. Jeon; Software, H. Zhao; Validation, H. Zhao, J. H. Jeon and Y. W. Lee; Formal Analysis, H. Zhao, J. H. Jeon and Y. W. Lee; Investigation, H. Zhao and J. H. Jeon; Resources, D. I. Yu and Y. W. Lee ; Data Curation, H. Zhao ; Writing—Original Draft Preparation, H. Zhao and J. H. Jeon ; Writing—Re-view & Editing, D. I. Yu and Y. W. Lee; Visualization, H. Zhao; Supervision, Y. W. Lee; Project Administration, Y. W. Lee; Funding

Acquisition, Y. W. Lee.

References

[1] L. Mauric, and S. Broomhall, “Leonardo da Vinci and fluid mechanics,” Annual Review of Fluid Mechanics, vol. 53, pp. 1-25, 2021.

[2] D. Jackson and B. Launder, “Osborne Reynolds and the publication of his papers on turbulent flow,” Annual Review of Fluid Mechanics, vol. 39, pp. 19-35, 2007.

[3] P. B. Beaudan and P. Moin, Numerical Experiments on the Flow Past a Circular Cylinder at Sub-critical Reynolds Number, Technical Report No. TF-62, Thermosciences Division, Department of Mechanical Engineering, Stanford University, Stanford, California, USA, 1994. [Technical Report]. Available: https://web.stanford.edu/group/tfsa/TF_reports/ TF-062_Beaudon.pdf.

[4] H. M. Zdravkovich, Flow Around Circular Cylinders: Volume I: Fundamentals, OUP Oxford, 1997.

[5] J. H. Lienhard, Synopsis of lift, drag, and vortex frequency data for rigid circular cylinders, Technical Extension Service, Washington State University Pullman, WA, 1968.

[6] T. Norberg, An experimental investigation of the flow around a circular cylinder: influence of aspect ratio, Journal of Fluid Mechanics, vol. 258, pp. 287-316, 1994.

[7] A. G. Kravchenko and P. Moin, Numerical studies of flow over a circular cylinder at ReD=3900, Physics of Fluids, vol. 12, no. 2, pp. 403-417, 2000.

[8] A. Benim, E. Pasqualotto, and S. Suh, “Modelling turbulent flow past a circular cylinder by RANS, URANS, LES and DES,” Progress in Computational Fluid Dynamics, An International Journal, vol. 8, no. 5, pp. 299-307, 2008.

[9] D. A. Lysenko, I. S. Evstafye, and K. E. Rian, “Large-eddy simulation of the flow over a circular cylinder at reynolds number 3900 using the OpenFOAM toolbox,” Flow, Turbulence and Combustion, vol. 89, no. 4, pp. 491-518, 2012.

[10] H. Zhang, J. -m. Yang, L. -f. Xiao, and H. -n. Lü, “Large-eddy simulation of the flow past both finite and infinite circular cylinders at Re = 3900,” Journal of Hydrodynamics, vol. 27, no. 2, pp. 195-203, 2015.

[11] S. Dong and G. E. Karniadakis, “DNS of flow past a stationary and oscillating cylinder at Re=1000,” Journal of Fluids and Structures, vol. 20, no. 4, pp. 519-531, 2005.

[12] B. Seyed-Aghazadeh and Y. Modarres-Sadeghi, “An experimental investigation of vortex-induced vibration of a rotating circular cylinder in the crossflow direction,” Physics of Fluids, vol. 27, no. 6, 2015.

[13] S. Mittal and B. Kumar, “Flow past a rotating cylinder,” Journal of Fluid Mechanics, vol. 476, pp. 303-334, 2003.

[14] P. Thakur, N. Tiwari, and R. P. Chhabra, “Flow of a power-law fluid across a rotating cylinder in a confinement,” Journal of Non-Newtonian Fluid Mechanics, vol. 251, pp. 145-161, 2018.

[15] W. Chen and C. -K. Rheem, “Experimental investigation of rotating cylinders in flow,” Journal of Marine Science and Technology, vol. 24, no. 1, pp. 111-122, 2018.

[16] J. Smagorinsky, “General circulation experiments with the primitive equations: I. The basic experiment,” Monthly weather review, vol. 91, no. 3, pp. 99-164, 1963.

[17] F. Nicoud and F. Ducros, “Subgrid-scale stress modelling based on the square of the velocity gradient tensor,” Flow, Turbulence and Combustion, vol. 62, no. 3, pp. 183-200, 1999.

[18] N. Arya and A. De, “Effect of grid sensitivity on the performance of wall adapting SGS models for LES of swirling and separating–reattaching flows,” Computers & Mathematics with Applications, vol. 78, no. 6, pp. 2035-2051, 2019.

[19] M. Kim, J. Lim, S. Kim, S. Jee, and D. Park, “Assessment of the wall-adapting local eddy-viscosity model in transitional boundary layer,” Computer Methods in Applied Mechanics and Engineering, vol. 371, 2020.

[20] P. Parnaudeau, J. Carlier, D. Heitz, and E. Lamballais, “Experimental and numerical studies of the flow over a circular cylinder at Reynolds number 3900,” Physics of Fluids, vol. 20, no. 8, 2008.

[21] OpenCFD Ltd., OpenFOAM v2012 User Guide, https://www.openfoam.com/documentation/user-guide, Accessed June 25, 2025.

[22] R. Wang, S. Cheng, and D. S. K. Ting, “Effect of yaw angle on flow structure and cross-flow force around a circular cylinder,” Physics of Fluids, vol. 31, no. 11, 2019.

[23] F. Cao, H. Lin, C. Sun, J. Li, and B. Jiao, “Aerodynamic performance of a rotating cylinder at Re = 8.215×10^5,” Physics of Fluids, vol. 37, no. 2, 2025.

[24] J. C. Hunt, A. A. Wray, and P. Moin, Eddies, streams, and convergence zones in turbulent flows, Studying Turbulence Using Numerical Simulation Databases, 2. Proceedings of the 1988 Summer Program, 1988.

[25] R. D. Knowles, M. V. Finnis, A. J. Saddington, and K. Knowles, “Planar visualization of vortical flows,” Proceedings of the Institution of Mechanical Engineers, Part G: Journal of Aerospace Engineering, vol. 220, no. 6, pp. 619-627, 2006.

[26] J. Jeong and F. Hussain, “On the identification of a vortex,” Journal of fluid mechanics, vol. 285, pp. 69-94, 1995.